Journal of Applied Physics

Temperature and ambient atmosphere dependent electrical characterization of sputtered $IrO_2/TiO_2/IrO_2$ capacitors

Cite as: J. Appl. Phys. **131**, 095301 (2022); https://doi.org/10.1063/5.0080139
Submitted: 29 November 2021 • Accepted: 13 February 2022 • Published Online: 01 March 2022

F. J. Maier, M. Schneider, A. Artemenko, et al.

Journal of Applied Physics ARTICLE scitation.org/journal/jap

Temperature and ambient atmosphere dependent electrical characterization of sputtered $IrO_2/TiO_2/IrO_2$ capacitors

Cite as: J. Appl. Phys. **131**, 095301 (2022); doi: 10.1063/5.0080139
Submitted: 29 November 2021 · Accepted: 13 February 2022 ·
Published Online: 1 March 2022

F. J. Maier,[1,a)] M. Schneider,[1] A. Artemenko,[2] A. Kromka,[2] M. Stöger-Pollach,[3] and U. Schmid[1]

AFFILIATIONS

[1]Institute of Sensor and Actuator Systems, TU Wien, Gusshausstraße 27-29, 1040 Vienna, Austria
[2]Institute of Physics, Czech Academy of Sciences, Cukrovarnická 10, 162 00 Prague 6, Czech Republic
[3]University Service Centre for Transmission Electron Microscopy, TU Wien, Wiedner Hauptstraße. 8-10, 1040 Vienna, Austria

[a)]**Author to whom correspondence should be addressed:** franz.maier@hotmail.com

ABSTRACT

Titanium dioxide (TiO_2) is a high-performance material for emerging device applications, such as in resistive switching memories, in high-k capacitors, or, due to its flexoelectricity, in micro/nano-electro-mechanical systems. Enhanced electrical properties of TiO_2 are ensured, especially by a careful selection of the bottom electrode material. Iridium dioxide (IrO_2) is an excellent choice, as it favors the high-k rutile phase growth of TiO_2. In this study, we introduce the fabrication of $IrO_2/TiO_2/IrO_2$ capacitors and thoroughly characterize their electrical behavior. These capacitors show a dielectric constant for low temperature sputtered TiO_2 of ~70. From leakage current measurements, a coupled capacitive–memristive behavior is determined, which is assumed due to the presence of a reduced TiO_{2-x} layer at the IrO_2/TiO_2 interface observed from transmission electron microscopy analyses. The memristive effect most probably originates from trapping and detrapping of electric charges in oxygen vacancy defects, which themselves can be generated and annihilated through an applied electric field, subsequently changing the resistance of the capacitor. The electric degradation type is identified as a filament-forming mechanism. Additionally, the temperature dependence of the leakage current is measured, demonstrating that the temperature behavior is strongly influenced by the ambient atmosphere. The latter dependency leads to the hypothesis that the oxygen evolution reaction of water incorporated in the IrO_2/TiO_2 interface passivates vacancies, thus significantly impacting the vacancy density in TiO_2 and, as a further consequence, the electrical performance.

I. INTRODUCTION

Specific metal oxides offer outstanding properties for capacitors that make them unique for future electronic applications. Such properties include a resistance that "remembers" the electric field history or a much higher permittivity (high-*k*) compared to commonly used silicon dioxide (SiO_2). One of the most intensively investigated high permittivity capacitor materials is titanium dioxide (TiO_2),[1–4] as it is cheap, readily available, and CMOS compatible. Its high relative permittivity of up to 130[5] makes it suitable for a new generation of high-*k* capacitors. Widely used low permittivity dielectrics, like SiO_2, have a lower maximum capacitance per area than TiO_2 as the thickness of the dielectric cannot be decreased indefinitely. At film thicknesses below 3 nm, electrons have a high probability to tunnel through the insulating material, causing high leakage currents.[6] Thin films with higher permittivity can be made thicker to suppress this parasitic tunneling current while having the same capacitance per area. High-*k* materials, for example, hafnium oxide, are also interesting for field-effect transistors as they show less leakage current, improved drive current, and enhanced circuit performance compared to standard gate oxide dielectrics.[7]

High permittivity is also beneficial for micro-electro-mechanical system (MEMS) applications, where TiO_2 can be integrated as an actuator material when exploiting the so-called flexoelectric effect, as we demonstrated most recently.[8] As the flexoelectric effect is the coupling of mechanical strain to an electric field gradient, a detailed

understanding of the electrical properties of TiO_2 is vital for flexoelectric MEMS. Not only It is essential to gain knowledge not only on how the electric field is distributed in the dielectrics to understand the physics of the flexoelectric effect but also on how the dielectrics degrades when an electric field is applied to exploit its full potential without increasing the probability for device failure.

Another property of TiO_2 makes this material interesting, namely, the memristive effect. Here, the resistivity depends on the electrical history of the material and can change both continuously and suddenly, depending on the type of memristor. TiO_2 was the first material where memristive properties have been reported and ever since has been in the focus of intensive research activities for the memristive effect.[9–15]

The electrode material choice is crucial as it strongly influences the microstructural properties and, consequently, the electrical behavior of the capacitor. In this work, we chose iridium dioxide (IrO_2) for several reasons. Iridium dioxide is a low resistivity oxide (<500 Ω cm) and acts as an excellent seed layer for the subsequent deposition of TiO_2 as the crystal structure of IrO_2 is of the same crystallographic class as TiO_2 in the rutile phase, where the small lattice difference of 0.086 Å in a/b axis direction provides a good lattice match between both crystal lattices. This favorable crystallographic growth results in a higher permittivity compared to other metal oxides. We have confirmed the crystallographic properties in previous studies, where we investigated the crystallographic properties of the reactively sputtered IrO_2/TiO_2 stack both in Bragg–Brentano and gracing incidence x-ray diffraction mode.[8,16] To the best of the authors' knowledge, there are no studies regarding the electrical properties of TiO_2 capacitors based on IrO_2 as an electrode material.

To characterize the physical mechanisms that dominate the electrical behavior of a metal–insulator–metal (MIM) capacitor, it is common to perform current–voltage (I–V) measurements at different temperatures, which are evaluated with standard models, e.g., thermionic emission (Poole–Frenkel and Schottky) or tunneling (direct tunneling and trap assisted tunneling). Although these models work well for most capacitor materials, applying these models to oxygen vacancy rich materials like high permittivity oxides, such as TiO_2, falls short. As the material changes its electrical properties with the applied electric field, the standard formulas fail to describe the transient and temperature-dependent behavior of the leakage current. Oxygen vacancies are the primary source of structural defects in high permittivity oxides and are directly linked to the leakage current level.[17] When applying an electric field, the oxygen vacancy density is not constant and depends on the electric field strength, temperature, and time. As a consequence, these vacancy defects can cause the formation of conductive filaments, resistance changes at the interface, modulation of a Schottky barrier, or oxygen exchange between electrode and insulator, depending on the materials in the capacitor.[18,19] Additionally, electrochemical processes, such as the interaction of water molecules, nitrogen, or carbon with the top surface, make the evaluation of such devices even more challenging.

In addition, oxygen vacancies are known to be connected to the flexoelectric effect, and it is assumed that these defects play an essential role in the electro-mechanical behavior of flexoelectric actuators.[20,21]

Through careful evaluation of leakage current measurements at different temperatures, by variation of the dielectric thickness values and by the exposure to ambient atmosphere in between deposition steps, an understanding of the underlying physical mechanisms was gained and is presented in this work. This knowledge, in turn, can be used for future investigations, such as a temperature-dependent evaluation of flexoelectrically excited MEMS cantilevers.

II. EXPERIMENTAL DETAILS

All films were deposited by reactive DC magnetron sputtering. As substrate, a phosphorus doped silicon wafer with a bulk resistivity of 50 Ω cm was used. The TiO_2 films were synthesized from a 6-in. titanium target in a pure O_2 atmosphere with a flow rate of 20 SCCM at a back pressure of 2 μbar, plasma power of 800 W, and a target–substrate distance of 65 mm. The IrO_2 electrodes were deposited from a 4-in. iridium target in an Ar/O_2 gas mixture (flow rates: 80/20 SCCM) at 60 μbar, 500 W, and 65 mm target–substrate distance. The TiO_2 film parameters were chosen to achieve both stoichiometry and a high degree of crystallinity. The IrO_2 parameters were optimized to stay below a maximum film stress of 500 MPa in pre-experiments to avoid delamination. In the first set of samples, the vacuum between the IrO_2 bottom electrode and the TiO_2 layer deposition was intentionally broken. The sample was exposed to the atmosphere for approximately 1 day before depositing the TiO_2 layer. Four different samples with varying TiO_2 thicknesses, namely, 50/100/150/200 nm, have been realized with the same parameters and bottom interface exposure to air. In the second set of samples, the IrO_2 bottom electrode and the TiO_2 layer were deposited consecutively without breaking the vacuum.

Circular pads were patterned with a diameter of 250 μm by a lift-off process serving as the top electrode. Subsequently, TiO_2 was partially etched with an SF_6/O_2 plasma to provide access to the bottom electrode. The current–voltage (I–V) characteristics were measured with a Keysight B2911A in a four-wire setup. The voltage is varied stepwise and kept constant for each step for a defined hold time, during which the current is measured in defined time intervals.

The chemical surface compositions of the top IrO_2 electrode and the TiO_2 film deposited on IrO_2 were characterized by x-ray photoelectron spectroscopy (XPS). The XPS spectra were obtained by an AXIS Supra photoelectron spectrometer (Kratos Analytical Ltd., UK) equipped with a hemispherical analyzer and monochromatic AlK_α x-ray source (1486.6 eV). Two additional monitor samples (i.e., IrO_2/TiO_2 and $IrO_2/TiO_2/IrO_2$) without breaking the vacuum between the films were fabricated for XPS measurements. Sputter deposition parameters for these samples were the same as for those investigated electrically.

Analytical measurements at the IrO_2/TiO_2 interface were performed using a TECNAI TF20 (scanning) transmission electron microscope (S/TEM) operated at 200 keV. For this purpose, the electron beam was converged to a diameter of 0.15 nm and scanned across the interface. Simultaneously, electron energy loss spectra (EELS) were recorded in each position of the scan in order to determine the energy loss near edge structure (ELNES) of the titanium L edge. The ELNES of an ionization edge is characteristic for the chemical environment of the probed atomic species. Consequently,

it provides information about the oxidation state. We made use of the ELNES to study the titanium oxidation state directly at the IrO_2/TiO_2 interface.

III. MATERIAL CHARACTERIZATION

From the SEM picture, given in Fig. 1, the sputtered TiO_2 shows a columnar microstructure. In our previous publication, x-ray diffraction analysis showed that IrO_2 and TiO_2 are present in the rutile phase.[8] The thickness values of the individual layers are 120 nm IrO_2, 100 nm TiO_2, and 120 nm IrO_2.

XPS analysis was performed to evaluate the surface composition and oxidation state of IrO_2 and TiO_2. The corresponding deconvolution of the oxygen peaks of the IrO_2 top electrode appears to be a triplet with a major peak at 530 eV (component C1), as shown in Fig. 2(a). The other two broad oxygen peaks are at 531.7 (component C2) and 532.5 eV (component C3).[22,23] In accordance with Freakley *et al.*, the C1 peak can be associated with IrO_2, while C2 is attributed to OH bonds and the C3 component to adsorbed water.[23,25,26] The additional peak at ~534.2 eV originates from moisture, i.e., oxygen in electrically isolated H_2O molecules.[24]

We also performed temperature stability measurements, where we heated the samples from room temperature to 350 °C, measuring the XPS spectrum at each temperature step *in situ*. The result can be found in S1 in the supplementary material. This measurement shows that the IrO_2 electrode is stable for the thermal measurement range from room temperature to 100 °C, especially as the leakage current measurements were performed in air and not under vacuum.

The O 1s XPS spectra revealed an oxygen peak associated with an H_2O bond. The concentration of these water associated oxygen bonds was measured to be of 3%–5% of all chemical bonds on the top surface of the IrO_2 electrode. For comparison, the deconvolution of O1s XPS spectra of TiO_2 deposited on IrO_2 resulted in three peaks: 530.5 eV (TiO_2 bond), 532 ± 0.2 eV (C–O bond), and 533 ± 0.2 eV (C–OH/TiO_x bond)[27,28] [see Fig. 2(b)]. In contrast to the top IrO_2 electrodes, the O 1s spectra of the TiO_2 surface deposited on IrO_2 do not have a bond at 534.2 eV associated with oxygen within a water molecule.

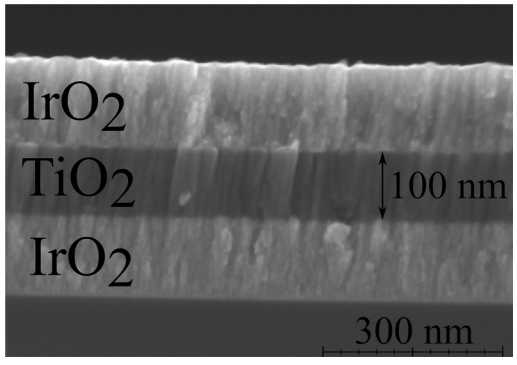

FIG. 1. SEM picture in cross-sectional view on an $IrO_2/TiO_2/IrO_2$ capacitor.

The TiO_2/IrO_2 interface of the bottom electrode was investigated by simultaneously recording STEM and EELS signals in STEM. The electron beam was focused to a diameter of 0.15 nm, and a scan box of 16 × 14 nm was drawn on the pre-recorded high angle annular dark-field (HAADF) STEM image as indicated in Fig. 3. The HAADF detector collects electrons being scattered at the atomic nuclei; thus, a bright signal is collected when the electron beam passes through high-Z materials, such as IrO_2. The recorded ELNES of the Ti–L edge is shown in Fig. 3. There is no ionization edge observed in the IrO_2 layer since the Ir and O edges are out of the detection range. The ELNES of TiO_2 is characteristic, like a fingerprint, and can thus be used for quantification of the respective sample area. We observe the typical ELNES of Ti^{4+} in TiO_2, being altered within an interfacial layer of 5.7 nm thickness. The Ti-ELNES from this interfacial layer indicates a strongly reduced state of titanium being due to an initial distribution of oxygen vacancies at the interface. The formation of these vacancies can be expressed in the Kröger–Vink notation,[29]

$$O_{\ddot{O}} \rightarrow V_{\ddot{O}} + 2e^- + \frac{1}{2} O_2,$$

where $O_{\ddot{O}}$ is the lattice oxygen and $V_{\ddot{O}}$ is a positively charged oxygen vacancy; here, Ö denotes a charged state. In TiO_2, these vacancy defects act as an n-type dopant.[12,30] This is due to oxygen having an oxidation number of −2 in TiO_2 and titanium having +4. For each oxygen atom missing, two bonds are unsaturated and contribute to the electrical conduction. There are different charge states of these vacancies (0, +, 2+), but for simplicity, we refer to these vacancies as V_0.

In Fig. 4, the band diagram of an $IrO_2/TiO_2/IrO_2$ capacitor is depicted. The work function of IrO_2 is typically around $\varphi_m \sim 4.2$ eV, and φ_s of TiO_2 can vary between 4.4 and 5.5 eV.[31,32] The electron affinity χ_a of TiO_2 is taken to be 3.9 eV.[33] From these values and the fact that V_0 vacancies act as n-type doping in TiO_2, an ohmic contact is expected. Even though the exact work function values of our samples are unknown, we can safely assume that a Schottky barrier does not form at this interface.

IV. CAPACITIVE BEHAVIOR

For the electrical material analysis of the $IrO_2/TiO_2/IrO_2$ capacitors, the capacitance is determined. In Fig. 5(a), the relative permittivity (χ_r), calculated from the impedance with a parallel capacitance–resistor equivalent circuit, can be seen. The permittivity values are in the range of 57–78 for 30–300 kHz. χ_r is almost independent of the film thickness, as only the 50 nm films show a slightly lower permittivity. These values are similar to, e.g., sputtered Al/TiO_2/Al MIM structures with an χ_r of ~60.[34] In Fig. 5(a), the relative permittivity of a 100 nm thick capacitor at varying temperatures is shown. There is a slight decrease in χ_r from 75 to 70 at 50 kHz over the temperature range from 25 to 100 °C.

V. TIME-DEPENDENT LEAKAGE CURRENT BEHAVIOR

To further understand the electrical behavior of the $IrO_2/TiO_2/IrO_2$ capacitors, leakage current measurements were performed. In Fig. 6, leakage current measurements at room temperature are shown

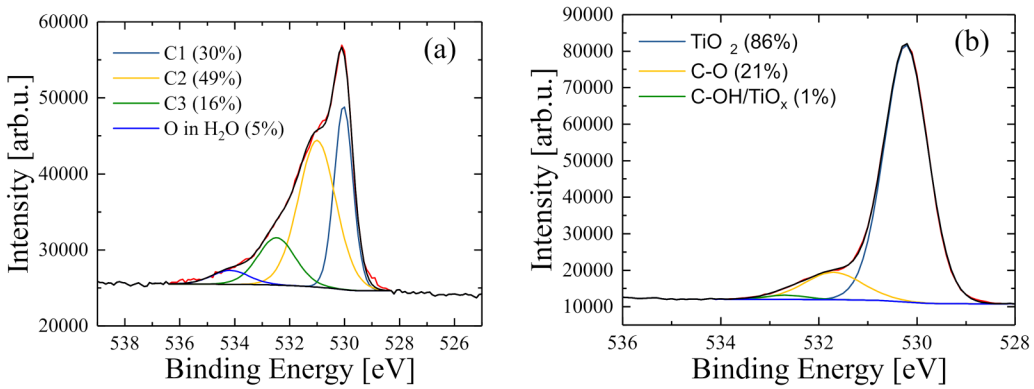

FIG. 2. The deconvoluted O 1s XPS spectra of (a) the top IrO_2 electrode of an $IrO_2/TiO_2/IrO_2$ capacitor and (b) TiO_2 on an IrO_2 film. All films have a thickness of 100 nm.

for 100 ms hold time while the current was recorded every 10 ms. The current value at 100 ms is then plotted in the I–V curve. The measurement cycle steps the voltage first from 0 to +3 V, then from +3 to −3 V, and finally back from −3 to 0 V.

In the leakage current measurements, a so-called non-pinched leakage current hysteresis is observed. This characteristic indicates a parallel equivalent circuit of a capacitor and a memristor, as modeled by Sun *et al.*[35] The term *non-pinched* refers to the effect that after an electrical stressing, the measured leakage current is not zero when the applied field is zero. This is due to an internal electric field that originates from the separation of negative and positive ions. In this case, it is most likely that the oxygen captures two electrons and gets negatively charged (O^{2-}), and the oxygen vacancies are getting positively charged (V_0) and thus are separated. A more detailed analysis can be found in S2 in the supplementary material.

The origin of the memristive effect will be described in the following. Space-charge-limited-current (SCLC) is expected due to the ohmic nature of both interfaces.[36] The SCLC mechanism is present when a large carrier injection from the electrodes is expected, which is reasonable for our low barrier ohmic interface. The SCLC mechanism has previously been shown for $Al/TiO_x/Al$, $Al/TiO_x/TiO_2/Al$ memristors as well as Al/TiO_2–nanowire/Ti.[37–39]

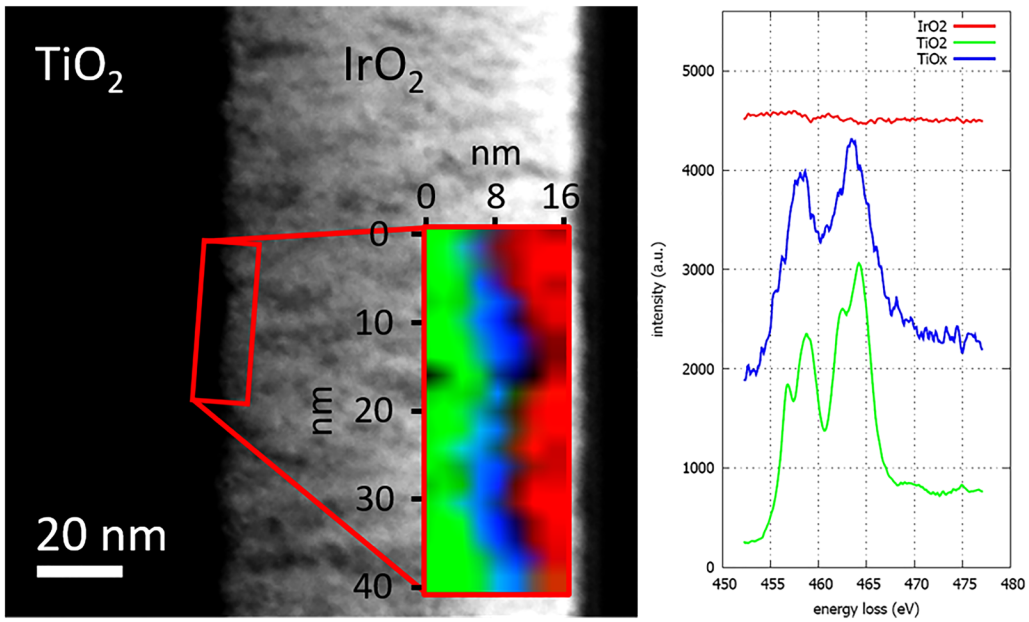

FIG. 3. STEM-EELS analysis of the bottom electrode/TiO_2 interface. From investigating the ELNES at the Ti–$L_{3,2}$ edge, an ~6 nm thick reduced TiO_{2-x} layer is detected.

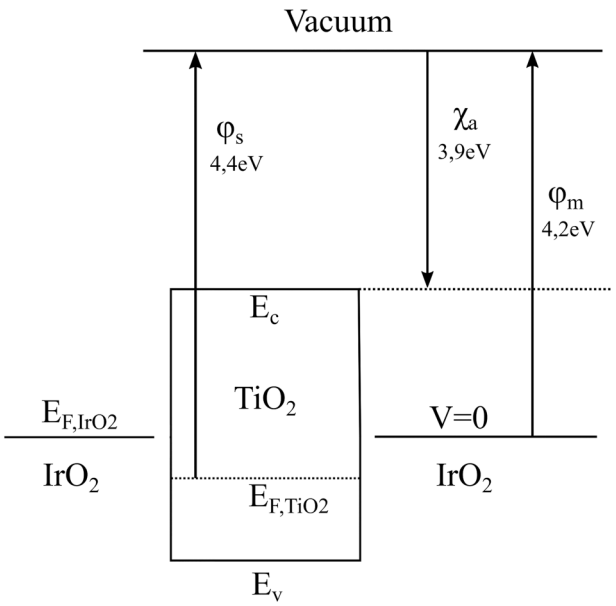

FIG. 4. Schematic band diagram for the $IrO_2/TiO_2/IrO_2$ capacitor before the materials are in contact. When the materials are brought into contact, the Fermi-energy $E_{F,TiO2}$ of TiO_2 is equalized with that of IrO_2 while the barrier height between IrO_2 and TiO_2 stays the same. This results in a downward bending of the conduction band of TiO_2, indicating the presence of an ohmic contact.

The Al/TiO_2 interface has a similar electronic structure as the IrO_2/TiO_2 interface with the work function of Al being ~4.06–4.28 eV, which should also form an ohmic contact.

To identify the leakage current behavior, two I–V measurements are done, one to a maximum of 1.2 V and the other to a maximum of 10 V. For both measurements, 20 measurement points with a hold time of 100 ms was chosen, in order to have similar total stressing times. From the measurement, as shown in Fig. 7(a), the slopes of the curve are initially close to 1 at low voltages (<1 V). A slope of 1 at low fields indicates ohmic behavior and can be described by the following equation:

$$J_{Ohm} = qn_0\mu\frac{V}{d},$$

where q is the elementary charge, n_0 is the free carrier density, μ is the carrier mobility, V is the applied voltage, and d is the thickness of the dielectric. In this regime, the time for the electrons to travel through the dielectric is higher than the dielectric relaxation time, meaning that the charge carriers have enough time to be distributed in such a way that the dielectric remains as charge neutral as possible. Hence, the number of injected carriers traveling across the insulator is small, and the thermal activation of the carriers exceeds the charge carrier injection mechanism. No traps are activated and the V_0 density is not changed, as depicted in Fig. 7(c).

At voltages above 1, the slope of the log I–log V curve is substantially higher, with ~17, which means that the voltage is higher than the transition voltage.[40] In this stage, the charge travel time is

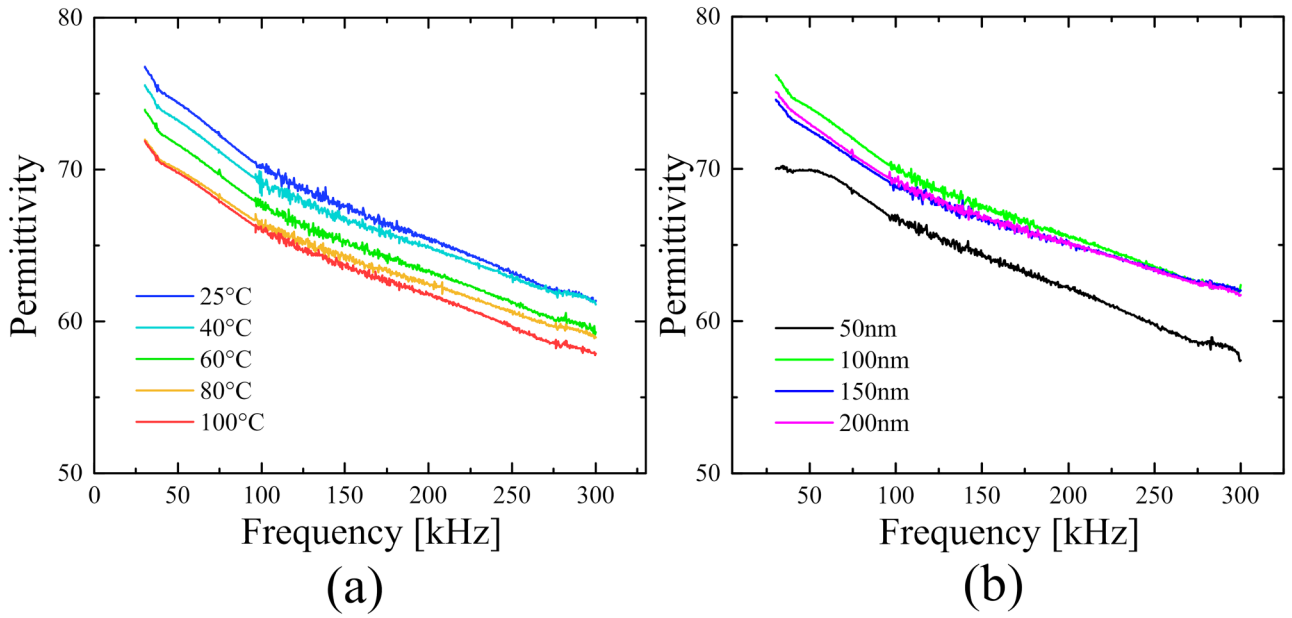

FIG. 5. (a) Permittivity vs frequency at different temperatures measured at test capacitors with a 100 nm thin dielectric TiO_2 layer. (b) Permittivity determined from impedance measurements vs frequency of $IrO_2/TiO_2/IrO_2$ capacitors with varying dielectric thickness. The sudden change in noise is due to a change in sensitivity in different measurement regions.

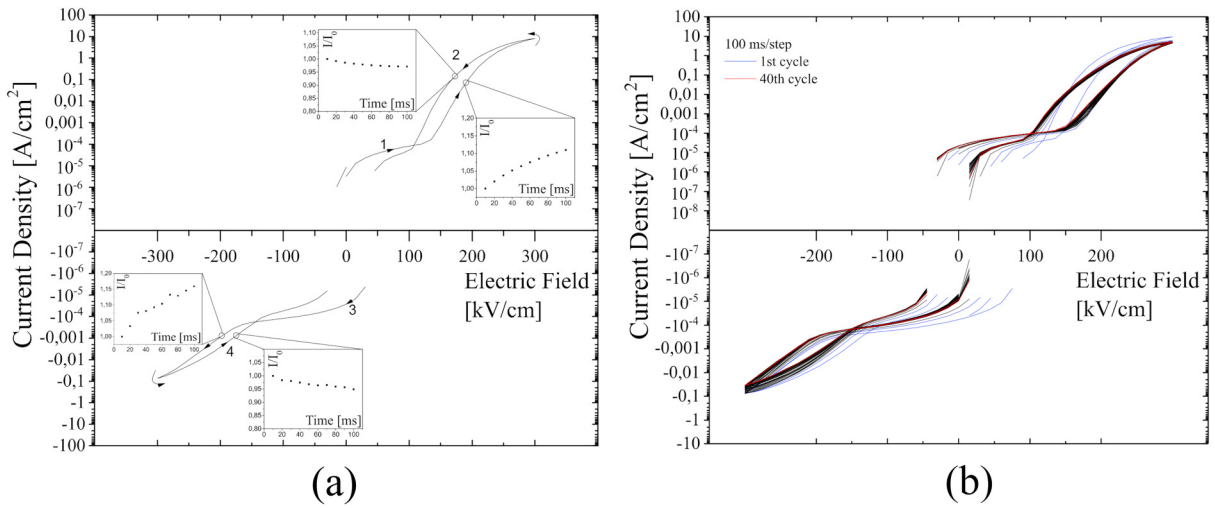

FIG. 6. Leakage current measurements of the capacitor. (a) 100 ms hold time for each measurement point. (b) 40 consecutive cycles of the I–V curve from (a). A non-pinched hysteresis is observed. The arrows indicate the direction of the voltage sweep. The insets show the current transient at each point during the hold time interval. The I–V curve is plotted as two separate logarithmic graphs, whereas at negative electric fields, the absolute values were plotted over a negative axis and flipped. Measurements were done in steps of 0.15 kV/cm.

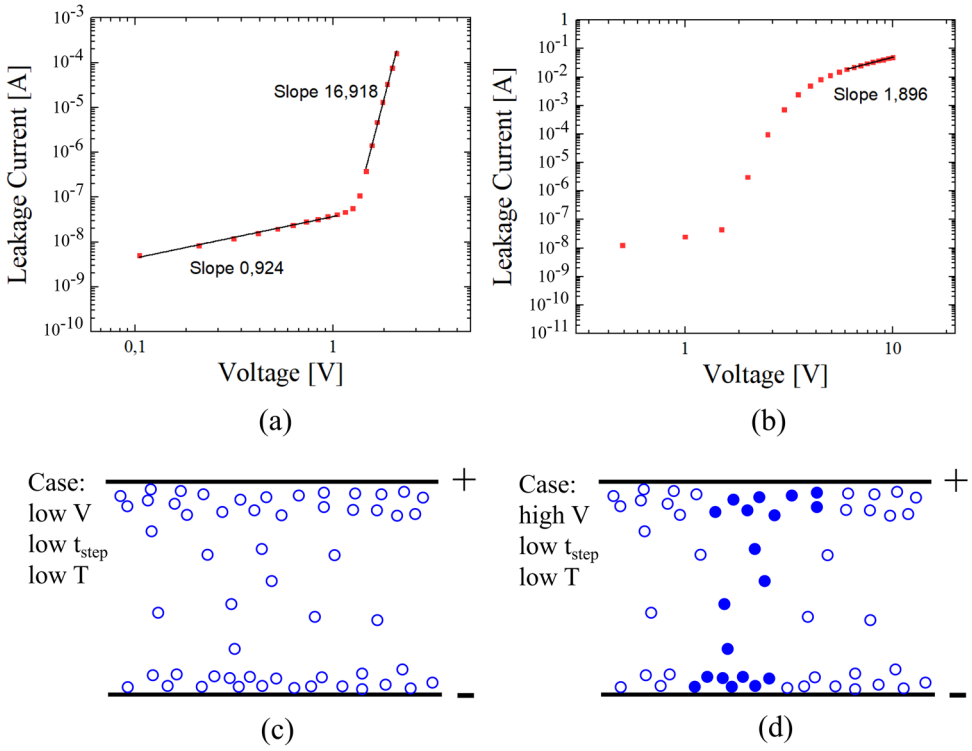

FIG. 7. (a) Log(I)–log(V) plot to identify the low voltage SCLC behavior (up to 2 V). One voltage sweep with 20 measurement points at 100 ms hold time at each step up to 1.2 V is shown. A slope of approximately 1 at voltages below 1 V, which is typical for ohmic conduction and a slope of approximately 17 at voltages from 1 to 1.2, can be identified. (b) Log(I)–log(V) plot to identify the high voltage SCLC behavior (up to 10 V). At higher voltages >4 V, a slope of approximately 2 can be seen. (c) Schematics of the capacitor with when a low voltage is applied. The intrinsically present amount of oxygen vacancies is shown as blue rings. (d) Schematic of the capacitor when a high voltage is applied. At higher biases, traps can be filled, preferably along low resistivity paths across the insulator. Filled traps are shown as blue circles.

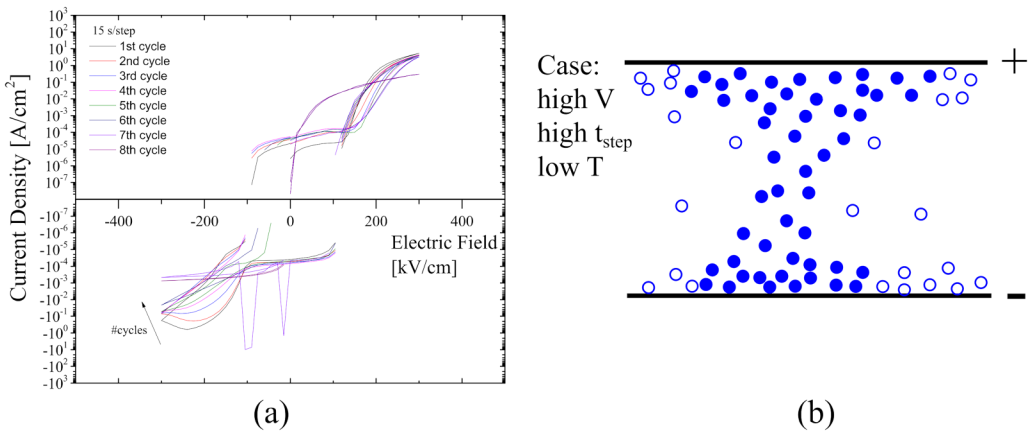

FIG. 8. (a) Repeated cycles at 15 s/step of a 100 nm thick capacitor. The measurement shows dynamic leakage current behavior, and, at higher cycles, the resistive switching and the capacitive hysteresis vanish, indicating the presence of a filament formed, as depicted in (b).

lower than the dielectric relaxation time and the electrons fill the traps, preferably along channels throughout the dielectrics [schematically shown in Fig. 7(d)].[41] Looking at the current transient in this regime [insets in Fig. 6(a)], an increase in current over time at a steady bias is observed. This shows that the traps are filled over time and the decrease in slope over time indicates that at some point all traps with energy corresponding to the bias voltage are filled. Once the traps are filled, they no longer excert a pushback force and the I–V behavior is transitioned to a trap-free SCLC behavior.[42] As seen from our measurements in Fig. 7(b), at voltages above 4, the slope is ∼2, which is in agreement with the trap-free SCLC Mott–Gurney law,

$$J_{Mott} = \frac{9}{8}\mu\varepsilon_0\varepsilon_r\frac{V^2}{d^3}.$$

It is also important to analyze the I–V behavior when sweeping from higher to lower voltage levels. Here, the current transient is negative [as shown in the insets in Fig. 6(a)], indicating that the traps are emptying over time. However, the internal electric field that comes from the capacitive effect affects the magnitude of the slope, and the leakage current mechanism in the reverse bias direction can, therefore, not be evaluated with a sufficiently high degree of certainty.

As in the case of trap filling and emptying, the memristive behavior is of electronic nature, and no significant change in the I–V behavior with subsequent cycles is expected. In Fig. 6(b), this measurement is shown and, indeed, no significant change is observed. Similar measurements were also performed at 1 ms hold time, which behave similar to measurements with 100 ms hold time.

It would be of interest to calculate the free carrier density and the carrier mobility. However, these values are dependent on the temperature and, as will be shown in Sec. VI, do not show the expected temperature dependence due to interfacial phenomena. As such, calculating n_0 and μ from Arrhenius plots is not possible.

To further analyze the behavior of the capacitors, a larger hold time at each voltage step was chosen, namely, 15 s.

At 15 s bias time, two big differences are identified. First, as seen in Fig. 8(a), the capacitively induced leakage current hysteresis shows a bigger internal field (I–V zero crossings at ±200 kV/cm compared to ±100 kV/cm for the 100 ms I–V curve). This is expected, as with longer bias time, the charge separation and, therefore, the internal field are increased. In general, the buildup internal electric field is rather large. There are only a limited number of studies that provide data about the induced electrical field strength. One study has reported a corresponding value of about 40 kV/cm, which is significantly lower.[43] To address this issue, understanding the exact origin of the capacitively induced hysteresis is certainly of interest but requests additional effort.

The second difference is that at negative bias direction, the behavior changed such that the memristive hysteresis is more pronounced and decreases even when the negative bias is increased. These changes can be explained by defect generation, which erodes low resistance paths in the insulator, leading to formed filaments, as depicted in Fig. 8(b).[41,44] When positive bias is applied, such filaments form, and when the bias is reversed, these channels break up, which can be seen in a significant decrease starting at −200 kV/cm even when the bias is further increased.[45] However, this is not stable resistive switching, and repeated cycles result in a decreased switching current, followed by sharp jumps in the current. Subsequently, both the capacitively induced hysteresis and the memristive hysteresis break down.[18] This breakdown is most likely related to a formed filament.

In the supplementary material S3, the transient I–V behavior at varying thickness is illustrated. The I–V curves for >50 nm thickness are similar, whereas the 50 nm sample is dominated by a capacitive leakage current hysteresis effect.

VI. TEMPERATURE-DEPENDENT LEAKAGE CURRENT MEASUREMENTS

For temperature-dependent characterization, two measurement cycles (two voltage cycles each) were performed subsequently at different temperatures ranging from 30 to 100 °C in air. At each

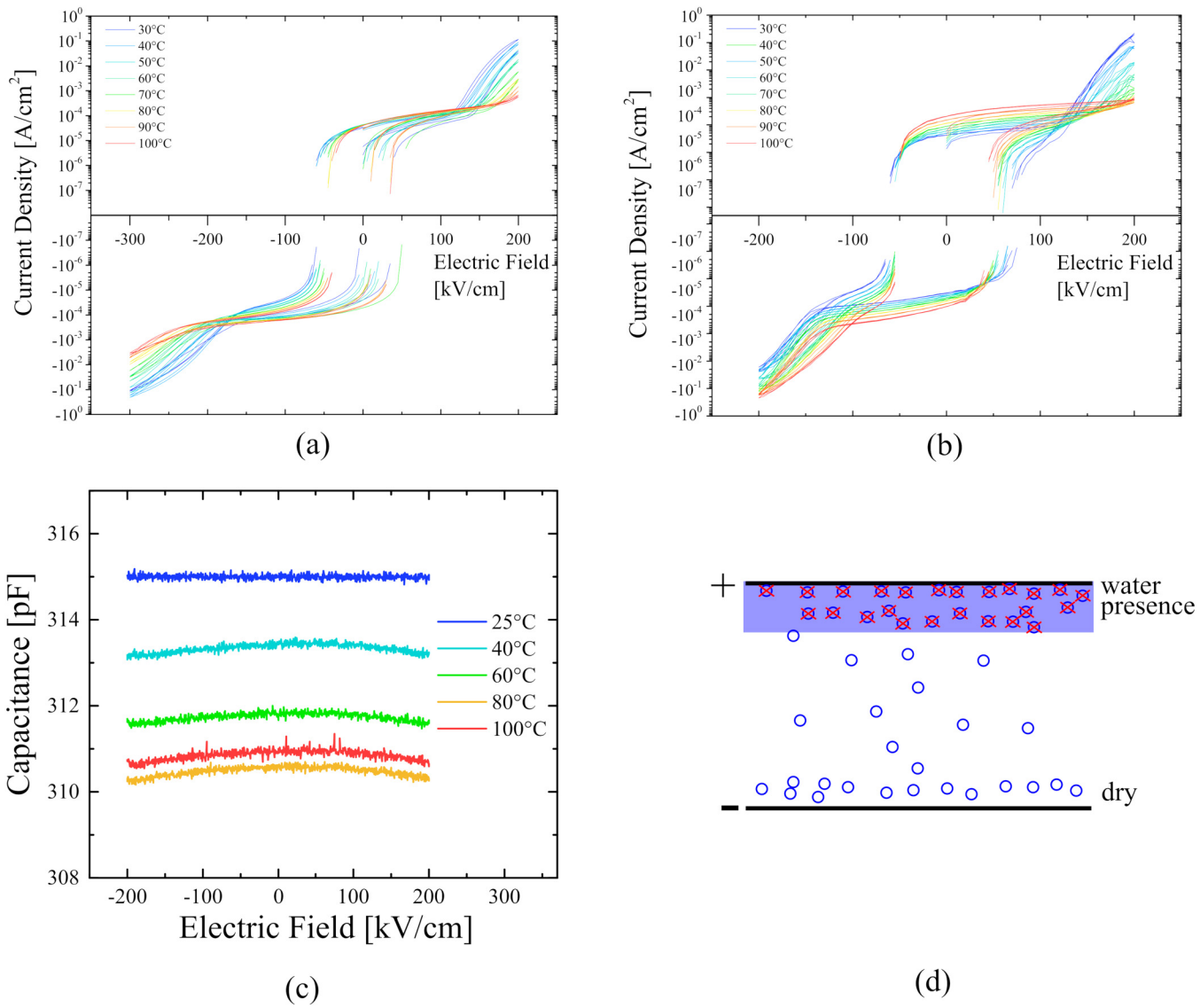

FIG. 9. Leakage current hysteresis measured at an $IrO_2/TiO_2/IrO_2$ capacitor with a top contact of 500 μm in diameter at varying temperatures. (a) shows measurements at a dielectric thickness of 100 nm with both bottom and top interfaces being exposed to the atmosphere while fabrication. (b) During sample synthetization, the vacuum was not broken between the bottom electrode and the TiO_2 layer deposition. This changed the behavior in the negative bias direction significantly, leading to an asymmetric dependence at a given temperature. (c) Capacitance–voltage values at 50 kHz of the sample with no atmosphere contact at the bottom interface, measured at different temperatures. (d) Schematics of the proposed mechanism responsible for the temperature dependence inversion. Blue circles are oxygen vacancies, the blue area indicates the presence of water, and the red cross a passivation of such a vacancy.

measurement point, the voltage was applied for a hold time of 100 ms before measuring the current value. For these measurements, the voltage limit is decreased. This is an attempt to avoid the filament forming and to stay in the pre-filament regime with the lowest amount of intrinsic changes possible. This seems to be the case for the samples with thickness of 100 nm as well as 150 and 200 nm, but not for 50 nm, as filament forming can be identified at a temperature of 70 °C and above, as shown in S4 in the supplementary.

To check if the capacitor is degrading with these measurement parameters, subsequent I–V cycles at a given temperature were measured. With the chosen measurement parameters, changes in the ≤100 nm capacitors are also reversible from one temperature to another. We performed measurements on a 100 nm sample where we

ramped up the temperature from 30 to 100 °C and then back down to 30 °C. The result, as shown in S5 in the supplementary material, demonstrated that the I–V curves in the heating-up phase are of similar behavior compared to those measured in the cooling down phase.

An interesting result of the performed I–V characterization, illustrated in Fig. 9(a), is the temperature-dependent behavior, where the memristive leakage current decreases with higher temperature, which is not expected, as the carrier mobility, free electron density, and oxygen vacancy forming rate should increase with temperature.[46,47]

This behavior can be explained when comparing it to the I–V characteristics of a sample where the vacuum between the bottom electrode and TiO_2 layer deposition was not broken [Fig. 9(b)]. For that sample, the current in the negative bias direction behaves differently than in the positive direction, even though the bottom and top electrodes are made from the same material with the same deposition parameters. In the positive bias direction, we measure a strongly decreasing leakage current by almost three orders of magnitude when moving to higher temperatures at sufficiently high electric fields (>100 kV/cm), similar to the sample from Fig. 9(a). This finding is not observed in the negative bias direction, where the leakage current increases by about one order of magnitude for increasing temperatures up to 100 °C independent of the electric field. This change from a symmetric temperature dependence (i.e., decreasing current density with increasing temperature at both bias directions) to an asymmetric temperature dependence (i.e., increasing current density with increasing temperature for negative bias when the bottom electrode surface was not exposed to air) leads to our assumption that the interface that is formed during air exposure is responsible for the unexpected temperature dependence of the leakage current.

There is still the possibility that the interface, which is expected to be ohmic, forms a Schottky contact. This Schottky contact could then be influenced by atmospheric exposure and change the barrier height accordingly. If this is the case for the results presented in Fig. 9(b), then a different barrier height for the bottom and top interface would lead to a diode-like behavior. We checked this with a capacitance–voltage (C–V) measurement at different temperatures, as illustrated in Fig. 9(c). The C–V curves show the expected constant relationship, and the capacitance changes ∼5 pF over the temperature range. This is strong evidence that Schottky behavior is not causing this behavior.

VII. INFLUENCE OF ATMOSPHERE ON THE INTERFACE

As we can see by the measurements in Figs. 9(a) and 9(b), the leakage current behavior is linked to the exposure of the interface between TiO_2 and bottom electrode during deposition to air, containing mainly nitrogen, oxygen, and humidity.

Assuming that oxygen diffused from the atmosphere into the surface, an oxygen density gradient is generated, which would lead to an equilibrium distribution over time, by decreasing the number of oxygen vacancies in IrO_2 and TiO_2. However, a capacitor stack oxidized to a higher degree would not lead to such a different temperature dependence of the leakage current, as a capacitor stack oxidized to a higher degree would lead to lower leakage currents in general, independent of temperature.

From the exposure to air, water is adsorbed on the IrO_2 surface.[48–51] From our XPS measurements, we identify OH and H_2O bonds at the surface of both IrO_2 and TiO_2, as explained in Sec. III. However, water has also been previously identified to have a strong influence on the electrical behavior, as shown by Jeong *et al.* for $Pt/TiO_2/Pt$ or by Messerschmitt *et al.* for $Pt/SrTiO_{3-\delta}/Pt$ capacitors.[43,52] It is known that when IrO_2 is exposed to water, hydroxyl bridges emerge at the surface.[51] Also, IrO_2 is one of the best catalysts for the aqueous oxygen evolution reaction (OER).[53,54] It was recently shown that when oxygen evolution reaction (OER) conditions are met, these hydroxyl bridges deprotonate, and the IrO_2 surface oxidizes.[55] At higher temperatures, the oxygen evolution rate of the IrO_2 electrode increases and more oxygen from the incorporated H_2O is available.[56] Similar behavior was also shown for $Nb:SrTiO_3/SrTiO_3/Pt$ capacitors.[57]

The drastic change in leakage current with temperature can then be explained with the Arrhenius-like dependency of the reaction rate of the OER. It has also been shown that IrO_2 has a decreasing linear change in the Tafel-slope regarding temperature.[58] Roughly speaking, the Tafel-slope can be related to an electrolytic cell efficiency. A decreasing Tafel-slope means an increase in the catalytic reaction rate.

Following this reasoning, the decrease in leakage current comes from the available oxygen from the deprotonation of the hydroxyl bridges at the interface. This additional oxygen can passivate oxygen vacancies and, therefore, change the vacancy density at the interface, schematically shown in Fig. 9(d). The decrease in vacancy density can then inhibit filament formation and conduction via low resistance channels, while still containing the push back field of the empty traps at the opposite interface. This is seen in a decreased leakage current when the interface was exposed to the atmosphere.

VIII CONCLUSIONS AND OUTLOOK

In this work, an in-depth experimental leakage current characterization of novel high-k $IrO_2/TiO_2/IrO_2$ capacitors is given. They show a wide variety of effects, such as vacancy formation and coupled capacitive–memristive effects. Experimental evaluation of the capacitance gives dielectric constant values of ∼70. The leakage current is dominated by capacitive effects at low fields, whereas at higher field regions, a memristive effect occurs. An ∼5 nm thick formed layer of reduced TiO_{2-x} at the IrO_2/TiO_2 interface is confirmed by TEM EELS measurements. The capacitively induced leakage current hysteresis most likely originates from the separation of negatively charged oxygen O^{2-} and positively charged oxygen vacancy V_0^+ when an electric field is applied. The memristive hysteresis at low hold times is predominantly due to the filling and emptying of oxygen vacancies along low resistivity channels across TiO_2. At higher hold times, V_0 density changes, making the channels thicker until filaments with metallic behavior are formed. The SCLC mechanism is expected due to the band structure of the interface and is confirmed by an analysis of the slopes of log(I)–log(V) curves. The filament-forming mechanism is confirmed by I–V measurements, where a breakdown of the capacitively induced I–V hysteresis indicates a connected filament. It was found that the filament forming is enhanced at certain conditions, such as lower film thickness, higher temperature, and longer sweep time.

Temperature-dependent measurements in the pre-filament-forming regime show an unexpected behavior in samples where the interface is in contact with the atmosphere. Here, the memristive leakage current decreases at higher temperatures. We fabricated samples where the bottom electrode surface was not in contact with air during fabrication. These samples show an asymmetric leakage current behavior, where the positive bias sweep shows a decrease in leakage current, but at a negative voltage sweep, the opposite behavior is measured. We argue that this is due to the deprotonation of OH bridges that form at the IrO_2/TiO_2 interface when in contact with air during deposition. This deprotonation results in oxygen atoms that can passivate the vacancies at the interface, inhibiting the ability to form filaments and subsequently decreasing the total leakage current.

SUPPLEMENTARY MATERIAL

See the supplementary material for additional information regarding the temperature stability of IrO_2 as well as low-field and thickness-dependent I–V curves of the capacitor structures. The authors acknowledge TU Wien Bibliothek for financial support through its Open Access Funding Programme.

AUTHOR DECLARATIONS

Conflict of Interest

This research received no external financial or non-financial support and there are no additional relationships to disclose.

DATA AVAILABILITY

The data that support the findings of this study are available from the corresponding author upon reasonable request.

REFERENCES

[1]J. Racko, M. Mikolášek, L. Harmatha, J. Breza, B. Hudec, K. Fröhlich, J. Aarik, A. Tarre, R. Granzner, and F. Schwierz, "Analysis of leakage current mechanisms in RuO_2–TiO_2–RuO_2 MIM structures," J. Vac. Sci. Technol. B **29**, 01AC08 (2011).

[2]M. Kadoshima, M. Hiratani, Y. Shimamoto, K. Torii, H. Miki, S. Kimura, and T. Nabatame, "Rutile-type TiO_2 thin film for high-k gate insulator," Thin Solid Films **424**, 224–228 (2003).

[3]B. Hudec, K. Hušeková, A. Tarre, J. H. Han, S. Han, A. Rosová, W. Lee, A. Kasikov, S. J. Song, J. Aarik, C. S. Hwang, and K. Fröhlich, "Electrical properties of TiO_2-based MIM capacitors deposited by $TiCl_4$ and TTIP based atomic layer deposition processes," Microelectron. Eng. **88**, 1514–1516 (2011).

[4]K. Fröhlich, J. Aarik, M. Ťapajna, A. Rosová, A. Aidla, E. Dobročka, and K. Hušková, "Epitaxial growth of high-κ TiO_2 rutile films on RuO_2 electrodes," J. Vac. Sci. Technol. B **27**, 266 (2009).

[5]B. Hudec, K. Husekova, E. Dobrocka, T. Lalinsky, J. Aarik, A. Aidla, and K. Frohlich, "High-permittivity metal-insulator-metal capacitors with TiO_2 rutile dielectric and RuO_2 bottom electrode," IOP Conf. Ser. Mater. Sci. Eng. **8**, 012024 (2010).

[6]G. He, Z. Sun, G. Li, and L. Zhang, "Review and perspective of Hf-based high-*k* gate dielectrics on silicon," Crit. Rev. Solid State Mater. Sci. **37**, 131–157 (2012).

[7]K. Mistry, C. Allen, C. Auth, B. Beattie, D. Bergstrom, M. Bost, M. Brazier, M. Buehler, A. Cappellani, R. Chau, C. Choi, G. Ding, K. Fischer, T. Ghani, R. Grover, W. Han, D. Hanken, M. Hattendorf, J. He, J. Hicks, R. Huessner, D. Ingerly, P. Jain, R. James, L. Jong, S. Joshi, C. Kenyon, K. Kuhn, K. Lee, H. Liu, J. Maiz, B. Mcintyre, P. Moon, J. Neirynck, S. Pae, C. Parker, D. Parsons, C. Prasad, L. Pipes, M. Prince, P. Ranade, T. Reynolds, J. Sandford, L. Shifren, J. Sebastian, J. Seiple, D. Simon, S. Sivakumar, P. Smith, C. Thomas, T. Troeger, P. Vandervoorn, S. Williams, and K. Zawadzki, "A 45nm logic technology with high-k+metal gate transistors, strained silicon, 9 Cu interconnect layers, 193nm dry patterning, and 100% Pb-free packaging" in *2007 IEEE International Electron Devices Meeting* (IEEE, 2007), pp. 247–250.

[8]F. J. Maier, M. Schneider, J. Schrattenholzer, P. U. Schmid, W. Artner, K. Hradil, A. Artemenko, and A. Kromka, "Flexoelectricity in polycrystalline TiO_2 thin films," Acta Mater. **190**, 124–129 (2020).

[9]A. Wedig, M. Luebben, D. Y. Cho, M. Moors, K. Skaja, V. Rana, T. Hasegawa, K. K. Adepalli, B. Yildiz, R. Waser, and I. Valov, "Nanoscale cation motion in TaO_x, HfO_x and TiO_x memristive systems," Nat. Nanotechnol. **11**, 67–74 (2016).

[10]B. J. Choi, D. S. Jeong, S. K. Kim, C. Rohde, S. Choi, J. H. Oh, H. J. Kim, C. S. Hwang, K. Szot, R. Waser, B. Reichenberg, and S. Tiedke, "Resistive switching mechanism of TiO_2 thin films grown by atomic-layer deposition," J. Appl. Phys. **98**, 033715 (2005).

[11]S. K. Kim, K. M. Kim, D. S. Jeong, W. Jeon, K. J. Yoon, and C. S. Hwang, "Titanium dioxide thin films for next-generation memory devices," J. Mater. Res. **28**, 313–325 (2013).

[12]D. B. Strukov, G. S. Snider, D. R. Stewart, and R. S. Williams, "The missing memristor found," Nature **459**, 1154 (2008).

[13]K. M. Kim, B. J. Choi, Y. C. Shin, S. Choi, and C. S. Hwang, "Anode-interface localized filamentary mechanism in resistive switching of TiO_2 thin films," Appl. Phys. Lett. **91**, 6–9 (2007).

[14]C. Rohde, B. J. Choi, D. S. Jeong, S. Choi, J. S. Zhao, and C. S. Hwang, "Identification of a determining parameter for resistive switching of TiO_2 thin films," Appl. Phys. Lett. **86**, 262907 (2005).

[15]Y. Sato, K. Kinoshita, M. Aoki, and Y. Sugiyama, "Consideration of switching mechanism of binary metal oxide resistive junctions using a thermal reaction model," Appl. Phys. Lett. **90**, 033503 (2007).

[16]F. J. Maier, M. Schneider, J. Schrattenholzer, and U. Schmid, "Electrical and microstructural characterization of TiO_2 thin films for flexoelectric devices," J. Phys.: Conf. Ser. **1837**, 012009 (2021).

[17]R. A. Parker and J. H. Wasilik, "Dielectric constant and dielectric loss of TiO_2 (rutile) at low frequencies," Phys. Rev. **120**, 1631 (1960).

[18]A. Sawa, "Resistive switching in transition metal oxides," Mater. Today **11**, 28–36 (2008).

[19]D. Cooper, C. Baeumer, N. Bernier, A. Marchewka, C. La Torre, R. E. Dunin-Borkowski, S. Menzel, R. Waser, and R. Dittmann, "Anomalous resistance hysteresis in oxide ReRAM: Oxygen evolution and reincorporation revealed by *in situ* TEM," Adv. Mater. **29**, 1700212 (2017).

[20]S. Das, B. Wang, Y. Cao, M. R. Cho, Y. J. Shin, S. M. Yang, L. Wang, M. Kim, S. V. Kalinin, L. Chen, and T. W. Noh, "Controlled manipulation of oxygen vacancies using nanoscale flexoelectricity," Nat. Commun. **8**, 615 (2017).

[21]D. Lee, A. Yoon, S. Y. Jang, J. Yoon, J. Chung, M. Kim, J. F. Scott, and T. W. Noh, "Giant flexoelectric effect in ferroelectric epitaxial thin films," **107**, 057602 (2011).

[22]M. Tariq, W. Q. Zaman, W. Sun, Z. Zhou, Y. Wu, L. M. Cao, and J. Yang, "Unraveling the beneficial electrochemistry of IrO_2/MoO_3 hybrid as a highly stable and efficient oxygen evolution reaction catalyst," ACS Sustainable Chem. Eng. **6**, 4854–4862 (2018).

[23]S. J. Freakley, J. Ruiz-Esquius, and D. J. Morgan, "The x-ray photoelectron spectra of Ir, IrO_2 and $IrCl_3$ revisited," Surf. Interface Anal. **49**, 794–799 (2017).

[24]J. V. Rojas, M. Toro-Gonzalez, M. C. Molina-Higgins, and C. E. Castano, "Facile radiolytic synthesis of ruthenium nanoparticles on graphene oxide and carbon nanotubes," Mater. Sci. Eng. B **205**, 28–35 (2016).

[25]S. J. Kerber, J. J. Bruckner, K. Wozniak, S. Seal, S. Hardcastle, and T. L. Barr, "The nature of hydrogen in x-ray photoelectron spectroscopy: General patterns from hydroxides to hydrogen bonding," J. Vac. Sci. Technol. A **14**, 1314–1320 (1996).

[26]H. Idriss, "On the wrong assignment of the XPS O 1s signal at 531–532 eV attributed to oxygen vacancies in photo- and electro-catalysts for water splitting and other materials applications," Surf. Sci. **712**, 121894 (2021).

[27]M. Drabik, A. Choukourov, A. Artemenko, J. Matousek, O. Polonskyi, P. Solar, J. Pesicka, J. Lorincik, D. Slavinska, and H. Biederman, "Aging of nanocluster Ti/TiO_x films prepared by means of gas aggregation cluster source," Surf. Coat. Technol. **205**, S48–S52 (2011).
[28]M. Drabik, A. Choukourov, A. Artemenko, O. Polonskyi, O. Kylian, J. Kousal, L. Nichtova, V. Cimrova, D. Slavinska, and H. Biederman, "Structure and composition of titanium nanocluster films prepared by a gas aggregation cluster source," J. Phys. Chem. C **115**, 20937–20944 (2011).
[29]D. S. Jeong, R. Thomas, R. S. Katiyar, J. F. Scott, H. Kohlstedt, A. Petraru, and C. S. Hwang, "Emerging memories: Resistive switching mechanisms and current status," Rep. Prog. Phys. **75**, 076502 (2012).
[30]J. J. Yang, M. D. Pickett, X. Li, D. A. A. Ohlberg, D. R. Stewart, and R. S. Williams, "Memristive switching mechanism for metal/oxide/metal nanodevices," Nat. Nanotechnol. **3**, 429–433 (2008).
[31]S. Kashiwaya, J. Morasch, V. Streibel, T. Toupance, W. Jaegermann, and A. Klein, "The work function of TiO_2," Surfaces **1**, 73–89 (2018).
[32]B. R. Chalamala, Y. Wei, R. H. Reuss, S. Aggarwal, B. E. Gnade, R. Ramesh, J. M. Bernhard, E. D. Sosa, and D. E. Golden, "Effect of growth conditions on surface morphology and photoelectric work function characteristics of iridium oxide thin films," Appl. Phys. Lett. **74**, 1394–1396 (1999).
[33]F. C. Marques and J. J. Jasieniak, "Ionization potential and electron attenuation length of titanium dioxide deposited by atomic layer deposition determined by photoelectron spectroscopy in air," Appl. Surf. Sci. **422**, 504–508 (2017).
[34]M. D. Stamate, "Dielectric properties of TiO_2 thin films deposited by a DC magnetron sputtering system," Thin Solid Films **372**, 246–249 (2000).
[35]B. Sun, Y. Chen, M. Xiao, G. Zhou, S. Ranjan, W. Hou, X. Zhu, Y. Zhao, S. A. T. Redfern, and Y. Norman Zhou, "A unified capacitive-coupled memristive model for the nonpinched current-voltage hysteresis loop," Nano Lett. **19**, 6461–6465 (2019).
[36]D. F. Barbe, "Space-charge-limited current enhanced by Frenkel effect," J. Phys. D: Appl. Phys. **4**, 1812–1815 (1971).
[37]M. Xiao, K. P. Musselman, W. W. Duley, and N. Y. Zhou, "Resistive switching memory of TiO_2 nanowire networks grown on Ti foil by a single hydrothermal method," Nano-Micro Lett. **9**, 1–9 (2017).
[38]S. Kim and Y. K. Choi, "A comprehensive study of the resistive switching mechanism in Al/TiO_x/TiO_2/Al-structured RRAM," IEEE Trans. Electron Devices **56**, 3049–3054 (2009).
[39]L. E. Yu, S. Kim, M. K. Ryu, S. Y. Choi, and Y. K. Choi, "Structure effects on resistive switching of Al/TiO_x/Al devices for RRAM applications," IEEE Electron Device Lett. **29**, 331–333 (2008).
[40]J. Pospisil, O. Zmeskal, S. Nespurek, J. Krajcovic, M. Weiter, and A. Kovalenko, "Density of bulk trap states of hybrid lead halide perovskite single crystals: Temperature modulated space-charge-limited-currents," Sci. Rep. **9**, 3332 (2019).
[41]Y. Yu, C. Wang, C. Jiang, I. Abrahams, Z. Du, Q. Zhang, J. Sun, and X. Huang, "Resistive switching behavior in memristors with TiO_2 nanorod arrays of different dimensions," Appl. Surf. Sci. **485**, 222–229 (2019).
[42]A. A. Petrov, N. V. Andreeva, and A. S. Ivanov, "Mechanism of electron transport and bipolar resistive switching in lead oxide thin films," AIP Adv. **8**, 105015 (2018).
[43]F. Messerschmitt, M. Kubicek, and J. L. M. Rupp, "How does moisture affect the physical property of memristance for anionic-electronic resistive switching memories?," Adv. Funct. Mater. **25**, 5117–5125 (2015).
[44]S. Abdelouahed and K. P. McKenna, "Relevance of non-equilibrium defect generation processes to resistive switching in TiO_2," J. Appl. Phys. **118**, 134103 (2015).
[45]G. Sassine, S. La Barbera, N. Najjari, M. Minvielle, C. Dubourdieu, and F. Alibart, "Interfacial versus filamentary resistive switching in TiO_2 and HfO_2 devices," J. Vac. Sci. Technol. B **34**, 012202 (2016).
[46]C. Mannequin, P. Gonon, C. Vallée, L. Latu-Romain, A. Bsiesy, H. Grampeix, A. Salaün, and V. Jousseaume, "Stress-induced leakage current and trap generation in HfO_2 thin films," J. Appl. Phys. **112**, 074103 (2012).
[47]F. Chiu, "A review on conduction mechanisms in dielectric films," Adv. Mater. Sci. Eng. **2014**, 578168 (2014).
[48]R. Martin, M. Kim, C. J. Lee, M. S. Shariff, F. Feng, R. J. Meyer, A. Asthagiri, and J. F. Weaver, "Molecular chemisorption of N_2 on IrO_2(110)," J. Chem. Phys. **152**, 074712 (2020).
[49]H. Hirakawa, M. Hashimoto, Y. Shiraishi, and T. Hirai, "Photocatalytic conversion of nitrogen to ammonia with water on surface oxygen vacancies of titanium dioxide," J. Am. Chem. Soc. **139**, 10929–10936 (2017).
[50]L. Huang, K. E. Gubbins, L. Li, and X. Lu, "Water on titanium dioxide surface: A revisiting by reactive molecular dynamics simulations," Langmuir **30**, 14832–14840 (2014).
[51]D. F. Abbott, D. Lebedev, K. Waltar, M. Povia, M. Nachtegaal, E. Fabbri, C. Copéret, and T. J. Schmidt, "Iridium oxide for the oxygen evolution reaction: Correlation between particle size, morphology, and the surface hydroxo layer from operando XAS," Chem. Mater. **28**, 6591–6604 (2016).
[52]D. S. Jeong, H. Schroeder, U. Breuer, and R. Waser, "Characteristic electroforming behavior in Pt/TiO_2/Pt resistive switching cells depending on atmosphere," J. Appl. Phys. **104**, 123716 (2008).
[53]D. R. Baker, M. B. Graziano, and B. M. Hanrahan, "Nanostructured antireflective iridium oxide coating for water oxidation," J. Phys. Chem. C **122**, 12207–12214 (2018).
[54]D. J. D. Matienzo, D. Settipani, E. Instuli, and T. Kallio, "Active IrO_2 and NiO thin films prepared by atomic layer deposition for oxygen evolution reaction," Catalysts **10**, 1–13 (2020).
[55]F. Nattino and N. Marzari, "Operando XANES from first-principles and its application to iridium oxide," Phys. Chem. Chem. Phys. **22**, 10807–10818 (2020).
[56]E. Nurlaela, T. Shinagawa, M. Qureshi, D. S. Dhawale, and K. Takanabe, "Temperature dependence of electrocatalytic and photocatalytic oxygen evolution reaction rates using NiFe oxide," ACS Catal. **6**, 1713–1722 (2016).
[57]T. Heisig, C. Baeumer, U. N. Gries, M. P. Mueller, C. La Torre, M. Luebben, N. Raab, H. Du, S. Menzel, D. N. Mueller, C. L. Jia, J. Mayer, R. Waser, I. Valov, R. A. De Souza, and R. Dittmann, "Oxygen exchange processes between oxide memristive devices and water molecules," Adv. Mater. **30**, 1800957 (2018).
[58]G. Zhang, H. Wang, J. Yang, Q. Zhao, L. Yang, H. Tang, C. Liu, H. Chen, Y. Lin, F. Pan, "Temperature effect on Co-based catalysts in oxygen evolution reaction," Inorg. Chem. **57** (2018) 2766–2772.